Spin-triplet supercurrents of odd and even parity in nanostructured devices

Lahabi, K.

4

CONTROLLING SUPERCURRENTS & THEIR SPATIAL DISTRIBUTION IN FERROMAGNETS

Kaveh Lahabi, Morten Amundsen, Jabir Ali Ouassou, Ewout Beukers, Menno Pleijster, Jacob Linder, Paul Alkemade & Jan Aarts

Spin-triplet Cooper pairs induced in ferromagnets form the centrepiece of the emerging field of superconducting spintronics. Usually the focus is on the spin polarization of the triplets, potentially enabling low-dissipation magnetization switching. However, the magnetic texture which provides the fundamental mechanism for generating triplets also permits control over the spatial distribution of supercurrent. Here we demonstrate the tailoring of distinct supercurrent pathways in the ferromagnetic barrier of a Josephson junction. We combine micromagnetic simulations with three-dimensional supercurrent calculations to design a disk-shaped structure with a ferromagnetic vortex which induces two transport channels across the junction. We use superconducting quantum interferometry to verify the presence of the two channels. Moreover, we show how the supercurrent can be controlled by moving the vortex with a magnetic field. This approach paves the way for current paths to be dynamically reconfigured in order to switch between different functionalities in the same device.

This chapter has been published in *Nature Communications* **8**, 2056 (2017).

Author contributions: K.L. and J.A. conceived the disk geometry, K.L. and E.B. performed the micromagnetic simulations. M.A., J.A.O. and J.L. performed the supercurrent simulations and assisted in the Fourier analysis. K.L. FIB-structured the devices, with guidance from P. A., K.L. and M.P. prepared the multilayers and performed the measurements.

4.1. INTRODUCTION

CONVERTING SPIN-SINGLET COOPER PAIRS TO EQUAL-SPIN TRIPLETS requires carefully designed interfaces between a conventional superconductor (S) and a ferromagnet (F) [1, 2]. As described in Section 3.1.2, this process requires both spin-mixing and spin-rotation, which can be brought about by magnetic inhomogeneities at the interface [3]. One method to realize this is to place a thin ferromagnet F' at the S/F interface, and make the magnetization of F and F' non-collinear [4]. This method was recently implemented in Josephson junctions described by 1D geometries, where the supercurrent amplitude was controlled by varying degrees of magnetic non-collinearity (MNC) [5–7]. This concept is illustrated in Figure 4.1 **a-b**. In this work we establish a different direction, where the focus is not the supercurrent amplitude. Instead, the central goal is to exert dynamic control over the triplet generator which in turn determines where the supercurrent spatially flows 4.1 **c**.

We demonstrate how distinct supercurrent paths in a device can be tailored entirely by spin texture, and altered in a dynamic fashion. Such behaviour is intrinsically higher-dimensional and can pave the way for novel hybrid devices in superconducting electronics.

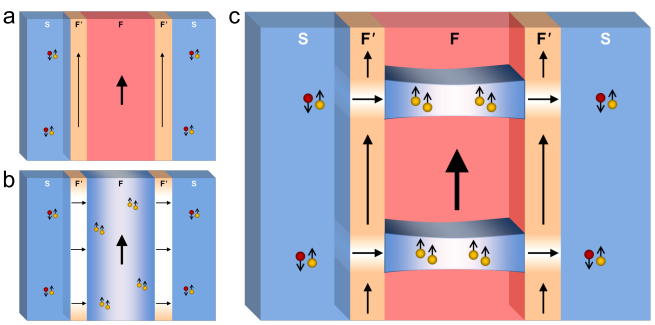

Figure 4.1: **a-b** Controlling the amplitude **a-b** and spatial distribution of supercurrent by the magnetic non-collinearity (MNC) in multilayers. **a** F and F' layers have a collinear magnetization, and the multilayer acts as a single homogenous ferromagnet. This corresponds to minimum junction transport since no long-range triplet current can be generated, and the singlet pairs are broken by the exchange field. Varying the magnetic orientation of the F' layers results in a long-range triplet current, which is maximum when F and F's are perpendicular (**b**). The singlet correlations however remain suppressed. **c** A 2D MNC profile is used to control the distribution of triplet supercurrent and form distinct transport channels.

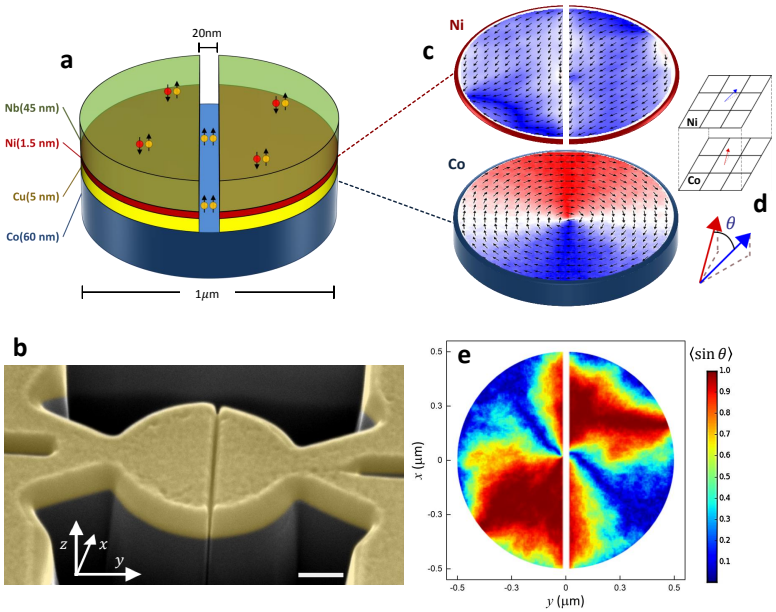

Figure 4.2: **Micromagnetic simulations and device layout**.**a**, Schematic of the device layout. **b**, False-colour scanning electron microscope image of a device. The scale bar corresponds to 250 nm. The disk is structured with Ga^+ focused ion beam (FIB) milling. The junction is formed by opening up a gap in the top Nb/Ni/Cu layers, leaving only Co in the weak link (see Methods for more details).**c**, Plane view of the magnetic states of Co and Ni layers in the disk (from 3-D OOMMF simulations). The pixel colour scheme, red-white-blue, scales with the magnetization along y. Magnetic moments in Ni tend to align with the gap which defines the junction, while the vortex configuration in Co arranges the magnetic moments perpendicular to it. This provides a high degree of magnetic non-collinearity (MNC) for triplet generation. The curled magnetic structure of the vortex is also highly effective in minimizing the stray fields from Co, which otherwise would dominate the Ni magnetization, hence compromising our control of MNC. **d**, Representation of our method to obtain the MNC profile. For each cell at the top of the Co layer, we determine the angle (θ) between its magnetization vector and that of the Ni cell above. **e**, Spatially resolved MNC profile calculated from the simulation results of shown in **c**. $<\sin(\theta)>$ is defined as the outer product between the Co and Ni magnetization vectors (note the colour scheme is different from **c**).The observed suppression of MNC (the blue region) at the centre of the junction is a result of interlayer dipole coupling at the vortex core.

4.2. RESULTS

4.2.1. MICROMAGNETIC SIMULATIONS

The device consists of a disk-shaped planar Josephson junction involving a multilayer of Co/Cu/Ni/Nb, as shown in Figure 4.2 **a**. A central trench cuts the top superconducting Cu/Ni/Nb layers in two halves, here connected via a Co weak link. The disk design combines two crucial elements. First, the magnetic moments in Co are arranged in plane and orthogonal to the trench between the superconducting electrodes, while the moments in Ni lie also in plane but parallel to the trench. Micromagnetic simulations show that this geometry results in a well-defined magnetic ground state with a high degree of MNC, a condition optimal for generating triplets

(Figure 4.2 **c** – **e**). An equally important element is that the disk shape creates a magnetic vortex state in the Co. This vortex produces a distinct suppression of MNC at the centre of the disk (Figure 4.2 **e**), which will be used to distribute the supercurrent in Co over two channels. The MNC suppression is due to the local out-of-plane magnetization at the vortex core, which turns the magnetic moments in the Ni also out-of-plane and, hence, collinear to the Co moments. Incidentally, the in-plane exchange field gradient of a magnetic vortex, without a second ferromagnet, has also been proposed to generate long-ranged triplets [8, 9]. This is the subject of Chapter 5, where we describe the nature transport in disk devices with no Ni layer.

4.2.2. SUPERCURRENT CALCULATIONS

To investigate whether a supercurrent can be expected, we numerically simulate the critical current density passing through the Josephson junction by solving the quasiclassical Usadel equation [10] in 3D using the magnetization texture obtained from the micromagnetic simulations. We do this by means of the finite element method, using the finite element library libMesh [11] in a similar fashion as in Ref. [12] (for details, please refer to Supplementary Note 1 of the original paper Ref. [13]). The superconductors are modelled as bulk, with a phase difference of $\Delta\phi = \pi/2$.

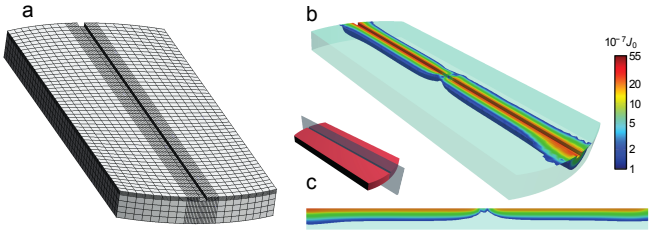

Figure 4.3: **Micromagnetic simulations and device layout**. **a** The discretized model (or mesh) used in the numerical simulation of the critical current. Since the triplet current is mostly concentrated in the immediate vicinity of the trench, the mesh density (and hence the accuracy) is set to be higher for this region. For the same reason, the regions farthest away from the trench have been removed to reduce the calculation time. **b** The critical current density divided by a factor $J_0 = (N_0 e D \Delta)/2\xi$ where N_0 is the density of states at the Fermi level, D is the diffusion constant, Δ is the superconducting gap and ξ is the superconducting coherence length. For clarity, currents lower than $10^{-7} J_0$ are not shown. **c** A slice through the centre of the trench, showing how the current passes across the Co barrier in two separate channels, on either side of the vortex core.

In Figure 4.3 **a** the discretized model is shown. To reduce the calculation time we truncated the otherwise circular geometry to a width of 40% of the disk diameter, as the currents farther away from the trench are negligible. The results are shown in Figure 4.3 **b**, **c**, where it can be seen that the critical current is suppressed at the centre of the disk, thereby effectively creating two separate current channels.

4.2.3. BASIC TRANSPORT PROPERTIES

As shown in Figure 4.4, our junctions show zero resistance and finite critical currents I_c below 3K The magnetic state of the sample was conditioned by applying a 2.5T out-of-plane field at 10K. This is to reduce the stochastic magnetization introduced by FIB milling of when structuring the junction.

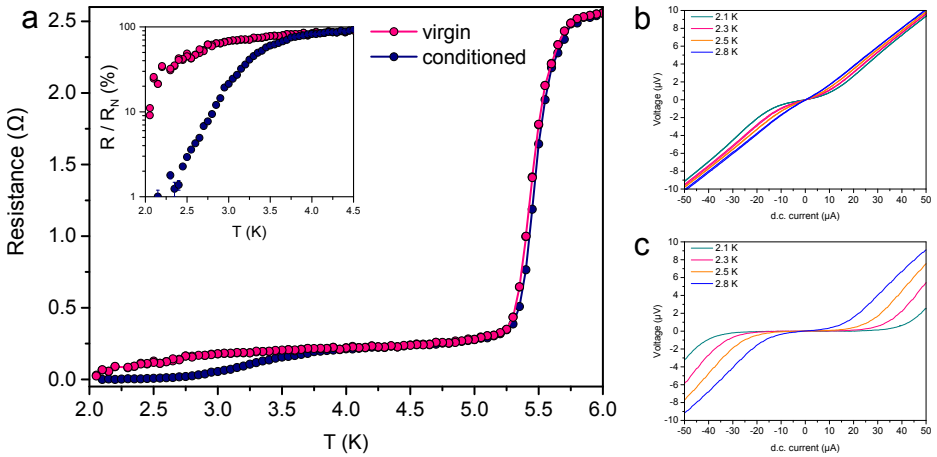

Figure 4.4: Junction transport in the virgin and conditioned states. **a** Resistance as a function of temperature, measured using 10 μA, before (pink) and after (navy) conditioning the sample. Each set shows two distinct transitions. At $T = 5.5$ K, the Nb electrodes become superconducting, while the junction is still in the normal state ($R_N \approx 240$ mΩ). Upon cooling further, resistance undergoes a second transition as the barrier begins to proximize by triplet correlations — eventually reaching zero resistance. For clarity, the $R-T$ dependence at lower temperatures is plotted on a logarithmic scale in the inset. While the superconducting electrodes are unaffected by conditioning the ferromagnets, we observe substantial enhancement of superconductivity in the barrier. **b** and **c** $I-V$ traces taken at several temperatures before and after conditioning the sample, respectively. The pronounced contrast between the two sets indicates that transport depends strongly on the magnetic configuration of the junction.

Figure 4.4 shows there is a strong difference with data taken before and conditioning the sample, which is a first indication that MNC and a triplet supercurrent are involved (also see Supplementary 4.5.2). For instance, conditioning allows the magnetic moments in Ni to rearrange more freely, and align with the gap opened by the FIB. This process increases the MNC in the vicinity of the barrier which, in turn, results in an enhancement of triplet supercurrent at zero field. A consequence of this can be found in the pronounced contrast between the $I-V$ traces measured before and after conditioning the magnetization, as shown in Figure 4.4 **b**, **c**.

4.2.4. SUPERCONDUCTING QUANTUM INTERFEROMETRY

To examine the spatial distribution of current density across our junctions, we apply an out-of-plane magnetic field B_z, and analyse the resulting supercurrent interference pattern. As demonstrated by Dynes and Fulton [14], the shape of such a super-

conducting quantum interference (SQI) pattern is given by the Fourier transform of the position-dependent critical current density across a junction $J_c(x)$ through

$$I_c(B_z) = \left| \int_{-R}^{R} dV J_c(x) e^{\frac{2\pi i L B_z x}{\Phi_0}} \right| \tag{4.1}$$

where L is the effective length of the junction, $2R$ is its lateral width (here the disk diameter), and $\Phi_0 = h/2e$ is the superconducting flux quantum. In a typical junction, the uniform distribution of supercurrent density ($J_c(x)$ =constant) leads to the well-known Fraunhofer interference pattern with a sinusoidal current-phase relation given by

$$\frac{I_c(B)}{I_{c0}} = \left| \frac{\sin\left(\frac{\pi\Phi}{\Phi_0}\right)}{\frac{\pi\Phi}{\Phi_0}} \right| \tag{4.2}$$

Characteristic for the Fraunhofer pattern is a central lobe that is twice as wide as the side lobes (as in Figure 4.5 **c**). These oscillations decay with a $1/B$ dependence. Different device configurations may introduce deviations from the standard pattern, but the described relative widths of the lobes persist as a common feature in all Josephson junctions, since it represents a single-slit interference pattern. In contrast, we expect our disk to exhibit a double-slit interference pattern. This is characterized by slowly decaying sinusoidal oscillations with Φ_0-periodicity, where all lobes have the same width. These patterns are typical for superconducting quantum interference devices (SQUIDs) which, contrary to our device, consist of two individual junctions operated in parallel.

As shown in Figure 4.5 **a**, **b**, the period of the oscillations in our disk device is 7.8 mT (i.e. fluxoid quantization over an effective area of 2.65×10^{-13} m^2, and appears to be temperature-independent. Qualitatively, the SQI patterns in Figure 4.5 **a**,**b** already foretell the presence of two supercurrent channels: the width of the central lobe is comparable to that of the side lobes, and the oscillations decay far more gradually in field than as $1/B$. Two-channel interference patterns were recently observed in junctions with topological weak links [15–17], where the two-slit interference is a result of edge-dominated transport caused by band bending. In our junction however, this is due to the suppression of triplet supercurrent by the (controllable) magnetic vortex core.

To illustrate the contrast with single-slit interference in a similar device configuration, we prepared a disk junction without the Ni layer, and retaining a thin layer of Cu/Nb at the bottom of the trench. This provides a non-magnetic path in the barrier, allowing singlet correlations to contribute to junction transport. Indeed, we observe a typical Fraunhofer-like interference pattern with a two times wider central lobe, shown in Figure 4.5 **c**. Provided that singlet current can dominate the transport, sim-

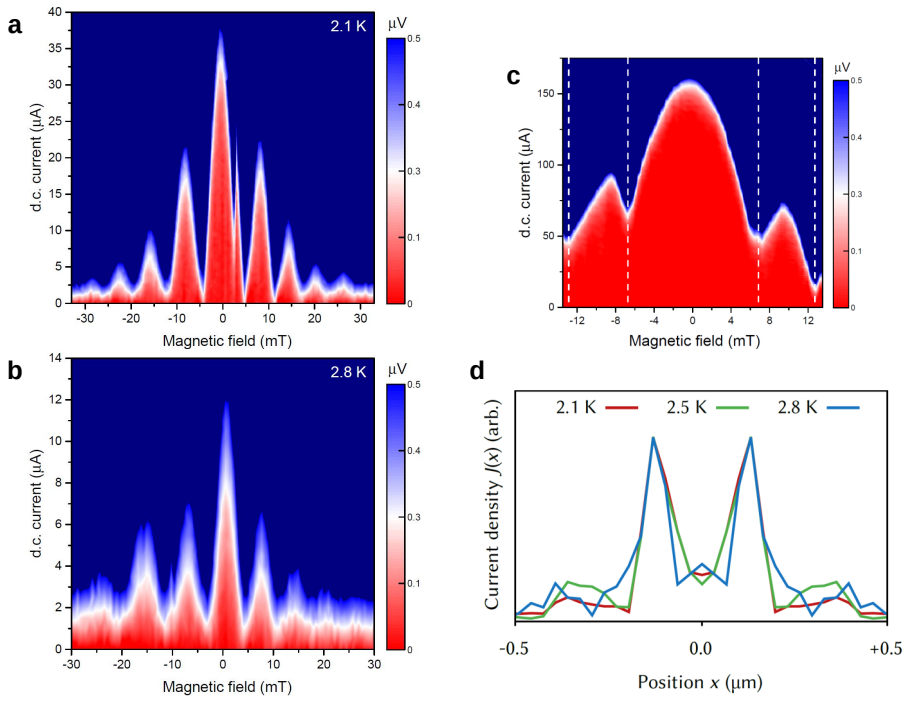

Figure 4.5: Interference patterns and the corresponding current density profiles. **a** and **a** the result of superconducting quantum interference (SQI) measurements taken at 2.1 K and 2.8 K respectively. The patterns show clear double-slit interference, with all lobes having the same width. **c** Single-slit interference pattern from a disk junction where transport is dominated by singlet correlations via a non-magnetic barrier. **d** The current density profiles constructed from the Fourier analysis of SQI patterns taken at 2.1 K , 2.5 K and 2.8 K. The presence of two transport channels, responsible for the SQUID-like interference patterns, is evident.

ilar results can also be produced in presence of the Ni layer (see Supplementary Figure 4.S5).

Figure 4.5 **d** shows the supercurrent density profiles extracted from Fourier analysis of the measured interference patterns. A description of this method can be found in Supplementary 4.5.4, but it should be mentioned that there is some arbitrariness in choosing the position of the sample edge if the effective junction length L is not known. We put the edge at the position where the current density goes to zero, which leads to a value for L of 170 nm. This is a reasonable number. For a homogeneous junction, taking 100 nm for λ_L of the Nb, L would be of the order of 220 nm. There is no reason however to expect very close agreement as discussed in Supplementary 4.5.4. Important is that for any choice of the edge position, two distinct transport channels are clearly visible in the extracted profiles. Comparing these results with the simulations, the supercurrents appear to follow narrower paths, located near the centre of the disk. We attribute this to current crowding effects, in which the neck-

shaped contacts and their sharp corners lead to a forward orientation of the currents. Note that in the electrodes, supercurrent distribution can only vary over a distance set by λ_L, which may explain why it does not simply fan out and form a uniform distribution along the trench.

It is important to note that the origin of the two-channel transport in our junction cannot be explained by singlet supercurrents in a doubly connected path. A direct evidence for this can be found in the SQI measurements taken before conditioning the sample (the virgin state). Let us suppose that two separate current paths were to form by accident during fabrication, and somehow made it possible for singlet correlations to bypass the Co layer via two symmetric channels (asymmetric channels cannot produce the well-defined nodes observed in the interference patterns). Had this been the case, the two channels must have already been present before conditioning the magnetic state, and the device would have behaved as a SQUID from the beginning. In contrast, despite several attempts, no sign of a double-slit interference was found in the virgin state (see Supplementary Figure 4.S1). The SQUID pattern only appeared when the magnetic state was properly conditioned to produce the intended MNC, designed specifically to generate two symmetric triplet channels. More details about the SQI measurements from the virgin state can be found in the Supplementary 4.5.2.

4.2.5. MAGNETOTRANSPORT WITH IN-PLANE FIELDS

Having established the principal role of MNC in shaping the supercurrent, we also examine the possibility of controlling them by altering the MNC profiles using an in-plane field B_y which moves the vortex along the trench Figure 4.6 **a** shows the measured critical currents $I_c(B_y)$ together with the micromagnetic MNC calculations for various stages during the (zero to positive) field sweep. In the first regime (shaded yellow), we modify the MNC profile by moving the vortex core along $+x$ towards the side of the disk. As the field is raised beyond 30 mT, we remove the vortex, thereby suppressing the supercurrent. The suppression of I_c in this regime (shaded blue) is caused by the antiparallel configuration of the ferromagnets, which occurs through the increase of stray fields from Co (now magnetized along $+y$) when the vortex leaves the disk. In the third regime (shaded green), Ni magnetization begins to reverse from negative to positive y direction, while Co remains magnetized along $+y$. At first, this process recovers I_c as a MNC re-emerges over the entire disk. As we increase the field however, the MNC begins to fade away as both layers magnetize along $+y$, resulting in a gradual suppression of I_c. Figure 4.6 **b** shows the variations in $I_c(B_y)$ when sweeping the field from a high positive to negative value, and back. We observe a complex pattern accompanied with a peculiar hysteresis, where individual features are mirrored (and not just shifted) with respect to the direction of field sweep.

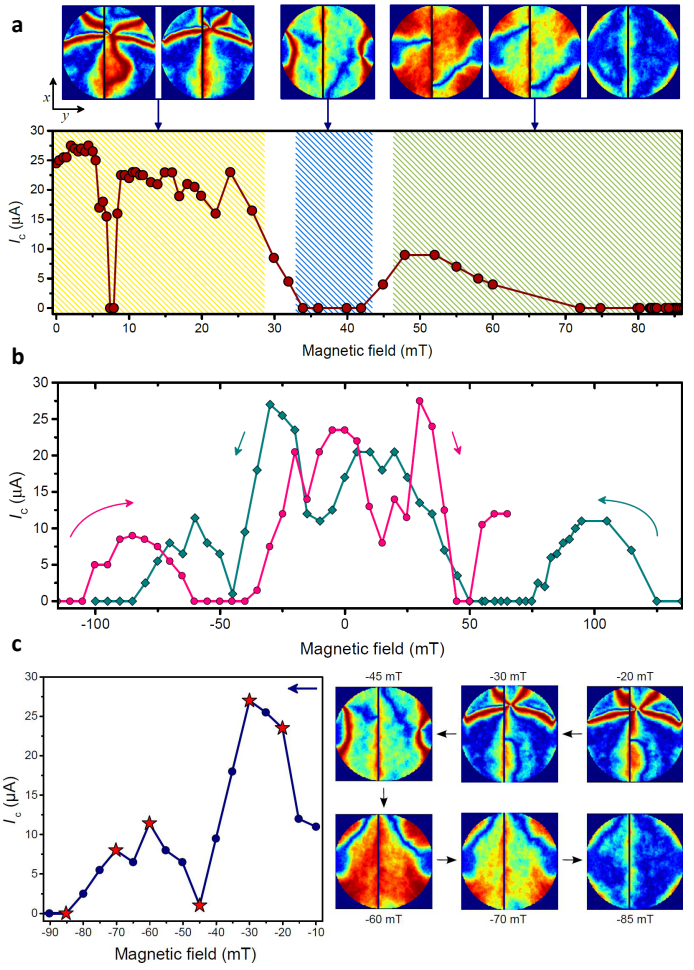

Figure 4.6: Critical current variation and MNC simulations with in-plane field. **a** Measured I_c values and the corresponding magnetic non-collinearity (MNC) profiles, as the system is magnetized by sweeping the field in $+y$ direction. For small fields the vortex core moves along the junction (perpendicular to field direction) to the side of the disk. In this range (shaded yellow), highly non-collinear regions are continuously present and appear to follow the position of the vortex core. The vortex state in Co, which has been effective in suppressing the stray fields, is subsequently removed as the field approaches 30 mT. This leads to a negative dipole field from Co which dominates the effective field acting on Ni. As a result, Ni gets magnetized antiparallel to Co (along $-y$), hence the suppression of MNC and I_c (shaded blue). As the applied field is raised above 45 mT , it begins to compensate for the local stray fields from the Co layer, ultimately reversing the Ni magnetization along $+y$. The change in the magnetic orientation associated with this reversal leads to a distinct (re-)emergence of MNC that gradually fades away above 60 mT - as Ni magnetization aligns with Co (shaded green). **b** I_c measured while reversing the field in both directions along y. A clear hysteresis is observed, with individual features are mirrored with respect to field sweep direction. This complex pattern is a result of a changing MNC as the multilayer reverses its magnetization. **c** Positive to negative branch of experimentally measured I_c (B_y) shown together with simulated MNC profiles. Each MNC snapshot is obtained at the specified field, and corresponds to a measurement labeled by the star symbol. Taking steps of 5 mT, simulation shows the vortex enters at -20 mT, moves along $-x$, and exits the system at -45 mT. The MNC is once again is enhanced at -60 mT, and gradually fades away as the field magnetizes all layers along $-y$.

The observed field dependence is fundamentally different from the usual hysteresis in SFS junctions, where the self-field of the ferromagnets can distort or introduce a shift in the interference pattern [18–20]. This is rather a distinct characteristic of triplet supercurrents produced by a varying degree of MNC, as the multilayer reverses its magnetization. The measured hysteresis is of a similar nature as the ones reported in Refs. [5, 6] for multilayer vertical stacks. The most notable difference here is arguably the relatively large field range where I_c is zero, and the pronounced reentrant superconductivity that follows. Figure 4.6 **c** compares one branch (positive to negative) of the measured $I_c(B_y)$ with the simulated MNC snapshots taken at various stages vortex reversal. Even though the experiment and the simulation both sweep the field in steps of 5 mT, the simulated fields for vortex entry and exit translate to direct enhancement and suppression of the measured I_c, respectively. For the fields below −45 mT, the behavior is similar to the one described for the third regime (green shade) in Figure 4.6 **a**.

As a final point, it should be noted that in the present letter we have assumed the channels have an equal phase. This assumption is reasonable for a symmetric MNC (hence spin-mixing) on each side [4]. Whether both channels are 0 or π, as long as they are symmetric, the SQI results will be indistinguishable. This would not strictly apply to systems with asymmetric spin texture (e.g. caused by vortex displacement), which can result in different phases for the triplet channels [9].

4.3. DISCUSSION

Spin-triplet supercurrents in ferromagnets have been bearing the promise of dissipationless use of spin-polarized currents. This study opens up a completely different direction, in which the focus is not the homogeneous amplitude of the supercurrent, but rather the dynamical control over its spatial distribution. This can lead to novel hybrid devices for superconducting electronics. Moreover, our extensive use of simulations, both of the micromagnetic configurations and of the supercurrents themselves, allow for detailed design and understanding before the actual fabrication of the hybrid device. The next step will be to introduce magnetization dynamics. Magnetic vortices or domain walls can be moved with pulses in the GHz regime, and this can also be simulated. Directing supercurrents then becomes possible on nanosecond timescales, opening the way for high-speed superconducting electronics.

4.4. METHODS

4.4.1. DEVICE FABRICATION

Multilayers of Co (60 nm)/Cu (5 nm)/Ni (1.5 nm)/Nb (45 nm) were deposited on unheated SiO_2-coated Si substrates by Ar sputtering in an ultrahigh vacuum chamber (base pressure below 10^{-8} Pa). The thickness of Co and the diameter of the disk (1 μm) are chosen to ensure stabilization of a magnetic vortex [21, 22]. The 5 nm Cu layer is used to avoid exchange coupling between the layers. The thickness of the Ni layer was tuned for optimal triplet generation in similar systems [20, 23]. The samples were subsequently coated with Pt (7 nm) to protect them from oxidation and to reduce the damage introduced by Ga^+ ions during focused ion beam (FIB) processing.

A combination of electron-beam lithography and FIB milling (50 pA Ga^+ beam current) was used to structure the disks. Next, FIB with 1 pA current was applied to open the sub-20 nm gap that forms the junction. The trench depth is controlled by the duration of milling. The 1 pA beam current provided sufficient timespan (several seconds) to vary the depth in a controlled manner. The device used for investigating single-slit transport was subject to the same processing steps, with the following exceptions. First, the multilayer was deposited without Ni to minimize triplet generation. Second, when creating the weak link, the duration of FIB milling was reduced by 20% to retain a layer of Cu/Nb at the bottom of the trench. This provides a non-magnetic path for singlet supercurrent in the weak link (on top of Co). The trench is presumably deeper near the sides of the disks (where sputtered atoms can escape more easily) than at the centre. Hence, in contrast to triplets, singlet correlations would favor the centre of the disk where a non-magnetic channel may still be present on top of the Co barrier.

4.4.2. MAGNETOTRANSPORT MEASUREMENTS

The magnetic properties of Co and Ni films used in our devices were characterized by ferromagnetic resonance experiments and SQUID magnetometry. Transport measurements were performed in a Quantum Design Physical Properties Measurement System where samples could be cooled down to 2.1 K. For both in- and out-of-plane measurements, the field was aligned within 2° of the sample plane. Resistance versus temperature was measured with a current of 10 μA. The current-voltage characteristics were taken in a four-probe configuration using a current-biased circuit and a nanovoltmeter. The critical current was determined using a voltage criterion: $V > 0.3$ μV for SQI and $V > 0.1$ μV for in-plane measurements.

The virgin state was measured directly after fabrication (Supplementary 4.5.2). Prior to the $I_c(B_z)$ measurements presented in the letter, the magnetic state of the sample

was conditioned by applying a 2.5 T out-of-plane field at 10 K. The sample was stored in a UHV chamber for 106 days and re-wired to a different puck, and the same measurements were repeated using a different magnet. We were able to reproduce the same Ic patterns, and no discernable changes in transport characteristics (e.g., $R(T)$ or I_c) were observed.

4.4.3. MICROMAGNETIC SIMULATIONS

The finite element micromagnetic calculations were carried out using the Object Oriented Micromagnetic Framework (OOMMF) [24]. The multilayer is divided into a three-dimensional mesh of 5 nm cubic cells. The exchange coefficient and saturation magnetization of Co were set to 30×10^{-12} Jm^{-1} and 1.40×10^{6} Am^{-1}, respectively, while for Ni these values were 9.0×10^{-12} Jm^{-1} and 4.90×10^{5} Am^{-1}. The Gilbert damping constant α was set to 0.5 to allow for rapid convergence. The direction of anisotropy was defined by a random vector field to represent the polycrystalline nature of the sputtered films. The Usadel calculations are based on static micromagnetic simulations of a multilayer disk with a diameter of 1 μm. For simulations with an applied in-plane field (shown in Figure 4.6), the disk design was extended to include the leads used for transport measurements in the actual device (Supplementary Figure 4.S2). In the absence of in-plane fields, the overall magnetic configuration remains relatively unaffected by the leads: the vortex core continues to suppress the MNC, resulting in two main channels for long-ranged triplet correlations. However, the influence of the leads on shape anisotropy becomes relevant when sweeping the field along y. This allows for an accurate estimate of the MNC, and the resulting variation in I_c during the magnetization reversal.

4.4.4. CONTROL EXPERIMENT

In addition to the device used for investigating the triplet currents, a control sample was prepared in parallel, on the same substrate. This was deposited together with the main device, and received the same treatment, with only one exception: the Ga^+ dose used for opening the gap that forms the weak link was lowered by 50%. Reducing the dose stops the milling before it reaches the Co layer in the trench. This leaves a non-magnetic path in the weak link for singlet correlations. The contribution of singlet supercurrent results in a critical current that is around 20 times higher than its neighboring junction (the main device) where the Co weak link can effectively suppress singlet correlations, hence allowing long-ranged triplet supercurrents to dominate the transport. Unlike triplets, the singlet current is not sensitive to the spin texture (i.e., MNC) of the system. This is evident from the single-slit (Fraunhofer-like) interference pattern, shown in Supplementary Figure 4.S5.

4.5. SUPPLEMENTARY INFORMATION

4.5.1. SUPPLEMENTARY FIGURES

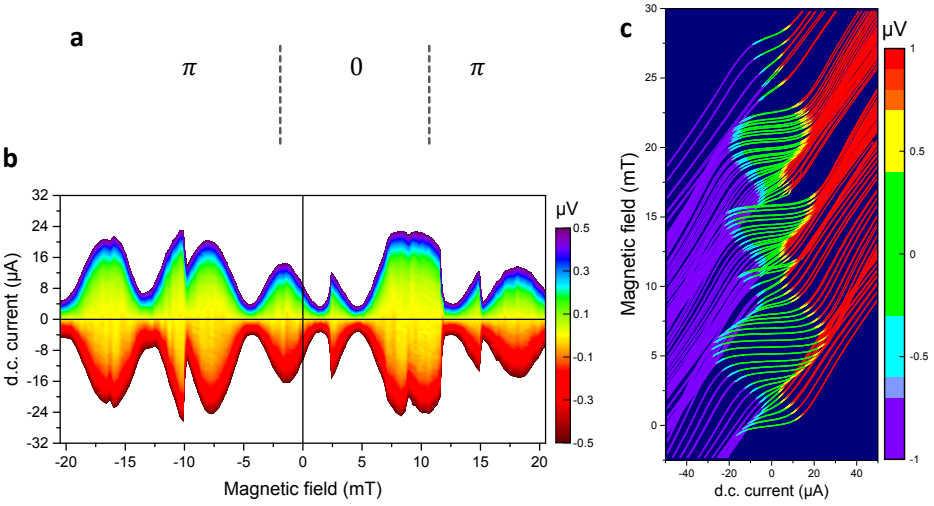

Figure 4.S1: Interference patterns from the virgin magnetic state. (a) Disordered magnetic state of Ni before conditioning (schematic). The stochastic magnetic orientation of Ni on each side of the trench can lead to the formation of multiple 0 and π segments across the junction. (b) Supercurrent interference pattern of the virgin magnetic state, measured while sweeping the out-of-plane field from negative to positive 30 mT in steps of 0.3 mT. On average, the supercurrent is suppressed for small fields (below 5 mT) in both field directions. The interference pattern is characterized by random discontinuities. These irregularities are shown more clearly in (c) which shows individual I-V curves taken while scanning the field from 28 mT back to zero. The curves are given an offset to represent the field they were measured at. All measurements are taken at $T = 2.1$ K.

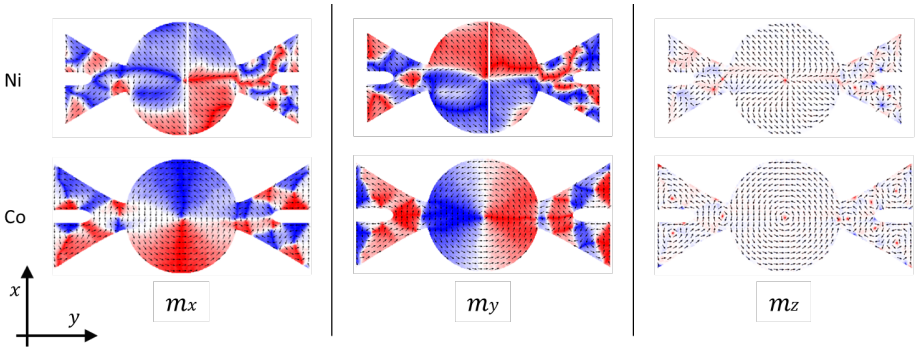

Figure 4.S2: Micromagnetic simulations with an in-plane field. Top views of the magnetic states of Co and Ni layers obtained from OOMMF simulations. The leads are included in the design to produce a more realistic shape anisotropy, needed to accurately describe the system under an in-plane field. Individual components of the magnetization vector $\boldsymbol{m}$ are plotted separately for clarity. The pixel colour scheme, red-white-blue, scales with the magnitude of each component. The red and blue pixels represent positive and negative values respectively. Out of plane magnetization (m_z) is generally suppressed, except at the vortex core where both layers have a highly localized out of plane component. In the actual device, the trench that forms the junction is slightly off-centred. This feature is accounted for in the simulations by placing the gap in Ni 40 nm away from the centre of the disk.

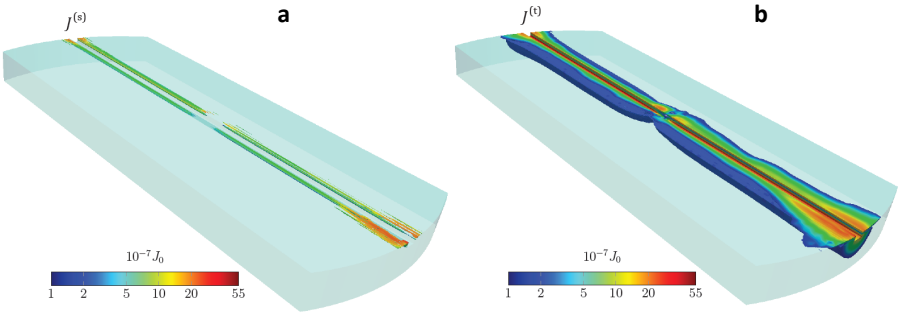

Figure 4.S3: Simulated contributions of singlet and triplet supercurrents. (a) Magnitude of the current density generated by singlet Cooper pairs, $J^{(s)} = |\boldsymbol{J}^{(s)}|$, which is greatly suppressed except for in the immediate vicinity of the superconductors. (b) Magnitude of the current density generated by triplet Cooper pairs, $J^{(t)} = |\boldsymbol{J}^{(t)}|$. For clarity, currents lower than $10^{-7}J_0$ have been removed, which explains why no singlet current is observed in the trench. It is noted that while the total current $\boldsymbol{J} = \boldsymbol{J}^{(s)} + \boldsymbol{J}^{(t)}$ is conserved, $\boldsymbol{J}^{(s)}$ and $\boldsymbol{J}^{(t)}$ are generally not. This is due to the magnetization, which causes oscillations between the singlet and triplet states.

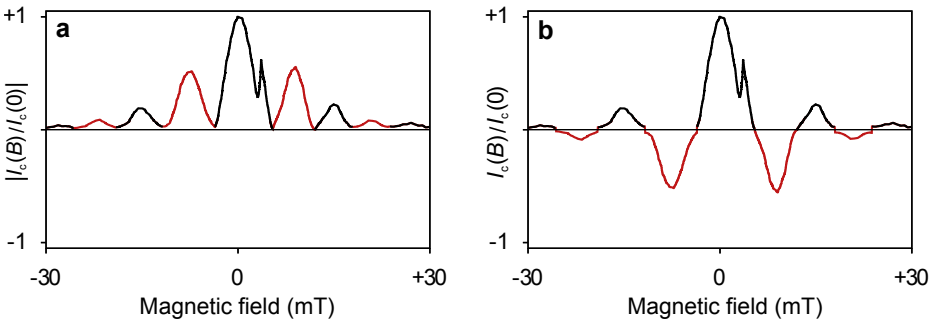

Figure 4.S4: Recovering the complex critical current. (a) The (unsigned) $|I_c(B)|$ pattern extracted from I-V measurements. (b) The signed $I_c(B)$ interference pattern reconstructed by flipping the signs of alternate lobes as in Ref [14]. The data were taken at 2.1 K.

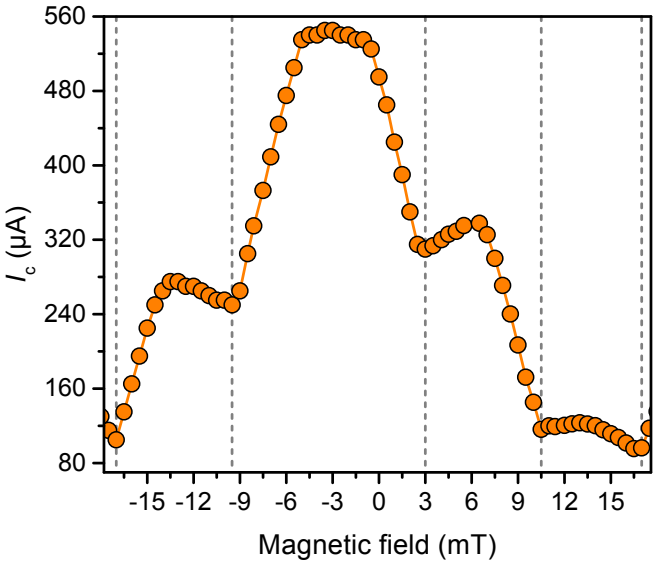

Figure 4.S5: Control experiment. Supercurrent interference pattern measured at $T = 2.1$ K from a control device that was processed in parallel with the one presented in the main text. Deposited together on one substrate, the same multilayer of Pt(7 nm)/Nb(45 nm)/Ni(1.5 nm)/Cu(5 nm)/Co(60 nm) was used in both devices. The Ga^+ dose applied in milling the weak link for the control device was reduced by 50 %. This provides a nonmagnetic pathway in the weak link, where singlet current is not suppressed, and can therefore dominate the transport. The result is a junction with a substantially higher critical current, showing single-slit interference pattern.

4.5.2. SUPPLEMENTARY NOTE 1: TRANSPORT IN THE VIRGIN STATE

Prior to conditioning the magnetization, supercurrent interference patterns were measured using small out-of-plane fields. These are presented in Figure 4.S1. In contrast to the conditioned sample, $I_c(B_z)$ is generally suppressed around zero field. We observe two maxima, which always occur at fields higher than 5 mT. Note that this offset cannot be attributed to remnant fields from the ferromagnet. The applied field for the interferometry measurements is not sufficient to have an appreciable influence on the magnetization of either layer. This is verified by SQUID magnetometry and ferromagnetic resonance experiments.

It has been proposed that the phase of triplet correlations in a S/F'/F/F'/S junction such as ours, is determined by the relative magnetic orientation of the F and F' layers on each side [25]. On the other hand, this unusual interference pattern, with two maxima and suppressed I_c at zero field, is the characteristic of a junction with multiple parallel 0 and π channels [26, 27]. This condition could be fulfilled in the virgin state, where the arbitrary orientation of Ni and Co magnetization can lead to random formation of multiple 0 and π segments across the junction. These interference patterns are also characterized by irregular discontinuities, which could be attributed to the arbitrary arrangement of the 0 and π segments.

Remarkably, we find these features to disappear altogether after conditioning the sample: $I_c(B_z)$ turns into a highly regular and reproducible SQUID pattern, with maximum I_c consistently appearing at $B_z = 0$. This pronounced dependence on magnetic conditioning was absent for junctions where singlet correlations dominated the transport: no significant changes in the interference pattern or the maximum value of I_c were observed.

4.5.3. SUPPLEMENTARY NOTE 2: NUMERICAL SIMULATIONS OF THE CRITICAL CURRENT

To calculate the critical current we use the quasiclassical approximation in the diffusive limit, which yields the Usadel equation [10]*

$$D\nabla\hat{\boldsymbol{g}}\nabla\hat{\boldsymbol{g}} + i\left[\hat{\boldsymbol{\rho}}_3 + \hat{\boldsymbol{\rho}}\cdot\boldsymbol{h}, \hat{\boldsymbol{g}}\right] = 0 \tag{4.3}$$

where D is the diffusion constant and ϵ is the quasiparticle energy. The magnetization texture from the micromagnetic simulations are represented as an exchange field $\boldsymbol{h} = \boldsymbol{h}(\boldsymbol{r})$. Furthermore we have defined $\hat{\boldsymbol{\sigma}} = \mathrm{diag}(\boldsymbol{g}, \boldsymbol{g}^*)$, where σ is a vector of Pauli matrices, and $\hat{\boldsymbol{\rho}}_3 = \mathrm{diag}(1,1,-1,-1)$. From $\hat{\boldsymbol{g}} = \hat{\boldsymbol{g}}(\boldsymbol{r},\epsilon)$, the 4×4 retarded Green function matrix in Nambu $\otimes$ spin space, the equilibrium current density may be

* The theoretical insights on supercurrent simulations were provided by Morten Amundsen, Jabir Ali Ouassou and Jacob Linder

computed as

$$\hat{\boldsymbol{J}} = \frac{N_0 eD}{2} \int \mathrm{d}\epsilon \, \mathrm{Re}\,\mathrm{Tr}\left(\hat{\boldsymbol{\rho}}_3 \hat{\boldsymbol{g}} \nabla \hat{\boldsymbol{g}}\right) \tanh\left[\frac{\beta\epsilon}{2}\right] \tag{4.4}$$

where N_0 is the density of states at the Fermi level, and $\beta = 1/(k_B T)$. We neglect the inverse proximity effect, and assume that the superconductors on each side of the trench are large enough to be approximated as bulk. In the calculations, we have used that the critical current is approximately found for a phase difference between the superconductors of $\Delta\phi = \pi/2$. For simplicity, we use transparent boundary conditions between the Ni and the Co layer, whereas we use the low-transparency Kupriyanov-Lukichev boundary conditions [28] at the Ni-Nb interface.

In the modeling of the geometry, we have assumed an effective superconducting coherence length of $\xi = 10$ nm, so that the radius of the circular disk becomes $R = 50\,\xi$. In the direction crossing the trench, the model has been truncated to a width of $W = 40\,\xi$ to reduce the model size. This has been done under the assumption that any contribution to the current from the removed regions is negligible due to the vast distance to the opposite superconductor. The thickness of the Ni and the Co layers have been set to ξ and $6\,\xi$, respectively, and the width of the trench is $2\,\xi$. The Ni thickness is set larger than in the actual experiment to avoid unnecessarily small elements in the Ni-region, which would substantially increase the calculation time. Although this yields lower values for the triplet current, the purpose of our calculation here is to identify the origin of this current; and not its absolute magnitude.

The spatial distribution of the magnetization in both the Ni and the Co layer are accurately mapped onto the 3D mesh via the exchange field $\hat{\boldsymbol{h}}$, where an amplitude of $|\hat{\boldsymbol{h}}| = 30\Delta \approx 46$ meV was used. While this is significantly lower than typical exchange fields in Co, it is still sufficient to quench the contribution of singlet Cooper pairs to the current density. To verify this, we make use of the fact that the supercurrent density generated by the singlet $\boldsymbol{J}^{(s)}$ and triplet $\boldsymbol{J}^{(t)}$ Cooper pairs contribute additively $J = \boldsymbol{J}^{(s)} + \boldsymbol{J}^{(t)}$. The two components are presented in Figure 4.S3 It is clear that the current density of singlet pairs rapidly vanishes away from the superconductors. In contrast, the triplet current density maintains an appreciable value over a substantially larger region, indicating that triplet Cooper pairs are the primary means of transport. The results will therefore be qualitatively the same for a more realistic strength of the exchange field. The advantage of using the reduced value is that the current densities become larger, which in turn make the numerical calculations less resource intensive.

The finite element analysis was carried out using 27-node hexagonal volume elements, and the Green function is interpolated within each element by means of second order Lagrange polynomials. This means that the current density within each element is interpolated by linear polynomials. To ensure that the spatial distribu-

tion of the current density is accurately resolved, we use a refined mesh in a region surrounding the trench, as is shown in Figure 4.3 **a** in the main text. For more details regarding the finite element analysis of three-dimensional superconducting heterostructures, please consult ref [12].

4.5.4. SUPPLEMENTARY NOTE 3: FOURIER ANALYSIS OF SUPERCURRENT DENSITY PROFILES

As shown by Dynes and Fulton1, the supercurrent density profile $J(x)$ can be determined from the superconducting interference pattern $I_c(B)$ using a Fourier transform:

$$J(x) \sim \int_{-\inf}^{+\inf} \mathrm{d}B \; I_c(B) \exp \frac{2\pi i L B x}{\phi_0} \tag{4.5}$$

Here, the coordinate system is defined such that the magnetic field B is applied along the z-axis, the critical current I_c is measured along the y-axis, and the current distribution J(x) can then be determined along the x-axis. The equation also depends on the effective length L of the junction and the flux quantum $\phi_0 = h/2e$. Note that $I_c(B)$ is the signed critical current, where the sign is determined from the experimentally measured $|I_c(B)|$ by assuming that it consists of alternating positive and negative lobes, as described in more detail in ref [14]. This procedure is justified when the interference pattern consists of well-defined maxima separated by deep minima, as is the case for our measurements.

The original method by Dynes and Fulton was derived for a rectangular junction where the dimensions of each superconductor are much larger than the London penetration depth λ. In that case, the effective junction length $L = 2\lambda + d$, where d is the thickness of the barrier between the superconducting leads. In our case, however, the junction is cylindrical and the current distribution not uniform, so the length (which determines the amount of flux to be screened) is not well defined. We therefore performed the Fourier analysis without making any assumptions regarding the value of L, but instead assumed that the position along the x-axis where we obtained $J(x) \to 0$ likely corresponded to the junction ends $x \approx \pm R$, where R is the cylinder radius. From this, we obtained an estimate $L \approx 180$ nm for the effective junction length. This value is somewhat lower than expected for a uniform rectangular junction: in that case the effective area is $2RL$ while the first minimum in $I_c(B_z)$ is at 7.8 mT, yielding $L \approx 270$ nm. Both numbers are of correct order of magnitude: the value of λ for a 50 nm Nb film is about 110 nm [29] so $2\lambda + d$ is 240 nm. If we were to take the sharp drop in the current density profile as the sample edge, L would become less than 100 nm, which appears to be too low in view of the value of λ.

The SQI experiments are carried out by measuring the voltage as a function of current for a given applied magnetic field, i.e. $V(I,B)$. The critical current $|I_c(B)|$, used for the Fourier analysis, is obtained by extracting a contour for a small but finite voltage threshold $V(I_c,B) > 0.3$ μV. Experimentally we find this criterion to be optimal for reducing noise effects that distort the shape of $I_c(B)$. The result is then adjusted to the y-axis so that $|I_c(B)| = 0$ at the nodes between the lobes of the interference pattern. This is to account for the artificial offset introduced by the 0.3 μV threshold voltage. We then recover the complex critical current $I_c(B)$, by switching the sign of every other lobe of the measured $|I_c(B)|$. The original $|I_c(B)|$ and the signed $I_c(B)$ curves are shown side-by-side in Figure 4.S4.

Note that the measured $I_c(B)$ may slightly deviate from a perfectly symmetric pattern, and yield a complex supercurrent distribution $J(x)$ after Fourier transformation. This apparent asymmetry however is predominantly caused by experimental noise. We therefore discard the complex phase $J(x)$ to approximate the supercurrent distribution profile by $|J(x)|$, shown in Figure 4.5 **d** of the main text.

REFERENCES

[1] M. Eschrig. Spin-polarized supercurrents for spintronics: a review of current progress. *Reports on Progress in Physics*, 78(10):104501, 2015.

[2] J. Linder and J. W. Robinson. Superconducting spintronics. *Nature Physics*, 11(4):307, 2015.

[3] F. Bergeret, A. Volkov, and K. Efetov. Long-range proximity effects in superconductor-ferromagnet structures. *Physical Review Letters*, 86(18):4096, 2001.

[4] A. I. Buzdin. Proximity effects in superconductor-ferromagnet heterostructures. *Reviews of Modern Physics*, 77(3):935, 2005.

[5] N. Banerjee, J. Robinson, and M. G. Blamire. Reversible control of spin-polarized supercurrents in ferromagneticJosephson junctions. *Nature Communications*, 5:4771, 2014.

[6] A. Iovan, T. Golod, and V. M. Krasnov. Controllable generation of a spin-triplet supercurrent in a Josephson spin valve. *Physical Review B*, 90(13):134514, 2014.

[7] W. M. Martinez, W. Pratt Jr, and N. O. Birge. Amplitude control of the spin-triplet supercurrent in S/F/S Josephson junctions. *Physical Review Letters*, 116(7):077001, 2016.

[8] M. Silaev. Possibility of a long-range proximity effect in a ferromagnetic nanoparticle. *Physical Review B*, 79(18):184505, 2009.

[9] M. S. Kalenkov, A. D. Zaikin, and V. T. Petrashov. Triplet superconductivity in a ferromagnetic vortex. *Physical Review Letters*, 107(8):087003, 2011.

[10] K. D. Usadel. Generalized diffusion equation for superconducting alloys. *Physical Review Letters*, 25(8):507, 1970.

[11] B. S. Kirk, J. W. Peterson, R. H. Stogner, and G. F. Carey. libMesh: a C++ library for parallel adaptive mesh refinement/coarsening simulations. *Engineering with Computers*, 22(3-4):237–254, 2006.

[12] M. Amundsen and J. Linder. General solution of 2D and 3D superconducting quasiclassical systems: coalescing vortices and nanoisland geometries. *Scientific Reports*, 6:22765, 2016.

[13] K. Lahabi, M. Amundsen, J. A. Ouassou, E. Beukers, M. Pleijster, J. Linder, P. Alkemade, and J. Aarts. Controlling supercurrents and their spatial distribution in ferromagnets. *Nature Communications*, 8(1):2056, 2017.

[14] R. Dynes and T. Fulton. Supercurrent density distribution in Josephson junctions. *Physical Review B*, 3(9):3015, 1971.

[15] S. Hart, H. Ren, T. Wagner, P. Leubner, M. Mühlbauer, C. Brüne, H. Buhmann, L. W. Molenkamp, and A. Yacoby. Induced superconductivity in the quantum spin hall edge. *Nature Physics*, 10(9):638, 2014.

[16] V. S. Pribiag, A. J. Beukman, F. Qu, M. C. Cassidy, C. Charpentier, W. Wegscheider, and L. P. Kouwenhoven. Edge-mode superconductivity in a two-dimensional topological insulator. *Nature Nanotechnology*, 10(7):593, 2015.

[17] M. T. Allen, O. Shtanko, I. C. Fulga, A. Akhmerov, K. Watanabe, T. Taniguchi, P. Jarillo-Herrero, L. S. Levitov, and A. Yacoby. Spatially resolved edge currents and guided-wave electronic states in graphene. *Nature Physics*, 12(2):128, 2016.

[18] V. Bol'ginov, V. Stolyarov, D. Sobanin, A. Karpovich, and V. V. Ryazanov. Magnetic switches based on Nb-PdFe-Nb Josephson junctions with a magnetically soft ferromagnetic interlayer. *JETP Letters*, 95(7):366–371, 2012.

[19] E. Gingrich, P. Quarterman, Y. Wang, R. Loloee, W. Pratt Jr, and N. O. Birge. Spin-triplet supercurrent in Co/Ni multilayer Josephson junctions with perpendicular anisotropy. *Physical Review B*, 86(22):224506, 2012.

[20] M. A. Khasawneh, T. S. Khaire, C. Klose, W. P. Pratt Jr, and N. O. Birge. Spin-triplet supercurrent in Co-based Josephson junctions. *Superconductor Science and Technology*, 24(2):024005, 2011.

[21] J. d. e Castro, D. Altbir, J. Retamal, and P. Vargas. Scaling approach to the magnetic phase diagram of nanosized systems. *Physical Review Letters*, 88(23):237202, 2002.

[22] N. Dao, S. Whittenburg, and R. Cowburn. Micromagnetics simulation of deep-submicron supermalloy disks. *Journal of Applied Physics*, 90(10):5235–5237, 2001.

[23] S. Voltan, A. Singh, and J. Aarts. Triplet generation and upper critical field in superconducting spin valves based on cro 2. *Physical Review B*, 94(5):054503, 2016.

[24] M. J. Donahue. OOMMF user's guide, version 1.0. Technical report, 1999.

[25] M. Houzet and A. I. Buzdin. Long range triplet Josephson effect through a ferromagnetic trilayer. *Physical Review B*, 76:060504, 2007.

[26] H. Smilde, D. Blank, G. Gerritsma, H. Hilgenkamp, H. Rogalla, et al. d-wave–induced Josephson current counterflow in $YBa_2Cu_3O_7$/Nb zigzag junctions. *Physical Review Letters*, 88(5):057004, 2002.

[27] C. Gürlich, S. Scharinger, M. Weides, H. Kohlstedt, R. Mints, E. Goldobin, D. Koelle, and R. Kleiner. Visualizing supercurrents in ferromagnetic Josephson junctions with various arrangements of 0 and π segments. *Physical Review B*, 81(9):094502, 2010.

[28] M. Y. Kuprianov and V. Lukichev. Influence of boundary transparency on the critical current of dirty SS'S structures. *Zh. Eksp. Teor. Fiz*, 94:149, 1988.

[29] A. Gubin, K. Il'in, S. Vitusevich, M. Siegel, and N. Klein. Dependence of magnetic penetration depth on the thickness of superconducting Nb thin films. *Physical Review B*, 72(6):064503, 2005.